

Extracting the parameters of two-energy-level defects in silicon wafers using machine learning models

Sijin Wang*, Brendan Wright, Yan Zhu, Yoann Buratti, Ziv Hameiri

UNSW, Sydney, New South Wales, 2052, Australia



ABSTRACT

This study introduces a pioneering machine learning (ML)-based methodology to characterise two-level defects in the bulk of silicon wafers. Bulk defects have a critical impact on the efficiency of silicon solar cells. By identifying the specific parameters of these defects, namely, their energy levels and capture cross-sections, researchers can devise strategies to mitigate their effects. It is often assumed that bulk defects are single-level defects following the Shockley-Read-Hall recombination statistics. However, two-level defects or even multi-level defects are common as well. At present, it is challenging to distinguish between single-level defects and two-level defects, and to extract the parameters of a two-level defect. This study proposes an ML-based approach to distinguish between one- and two-level defects based on temperature- and injection-dependent lifetime spectroscopy with an accuracy above 90 %. Furthermore, if the defect is identified as a two-level defect, this study presents another ML method to extract its defect parameters, with a correlation coefficient above 0.9 for the energy levels.

1. Introduction

A fast transition into green energy technologies, particularly photovoltaic (PV), is a crucial strategy to combat climate change [1]. The current PV market is dominated by silicon (Si)-based solar cells [2]. While the cost of Si-based PV systems has been significantly reduced in the last decade [2], there remains a necessity to further decrease their costs to exploit their full potential. As the cost associated with the balance of the system (BOS) represents a significant part of the total system's cost [3], improving the system efficiency is a promising path to make PV-generated electricity cheaper, as often the BOS cost is related to the number of PV modules. Presently, one of the main limitations of Si-based solar cells is defects in the Si wafers [4–7].

High concentrations of defects in the wafers (bulk defects) can significantly reduce the excess carrier concentration (Δn) at a given illumination condition [8]. As the open-circuit voltage (V_{oc}) [9] is directly related to Δn , bulk defects can reduce the V_{oc} of solar cells:

$$V_{oc} = \frac{k_B T}{q} \ln \left[\frac{(n_0 + \Delta n)(p_0 + \Delta n)}{n_i^2} \right], \quad (1)$$

where k_B is the Boltzmann's constant, T is the temperature, q is the electron charge, p_0 (n_0) is the equilibrium hole (electron) concentration, and n_i is the intrinsic carrier concentration [10]. As V_{oc} has a strong impact on the obtained fill factor (FF) [11,12], bulk defects also affect FF.

The significant advancement of surface [13] and contact [14,15] passivation in modern solar cells has led to increased attention to bulk recombination [16]. Since intrinsic recombination mechanisms, Auger and radiative [10,17], often have only minimal impact on the performance of Si wafers, recombination via defects has a critical impact on the bulk lifetime [18] as the defect energy states in the bandgap facilitate strong electron-hole recombination [10]. The origin of bulk defects varies and is impacted by contaminations during the ingot growth and the cell fabrication processes [19]. Identifying these defects is crucial to eliminating or at least minimising their detrimental effects.

Bulk defects can be categorised as either one-level or multi-level defects [18]. As indicated by the name, one-level defects have a single defect energy (E_d), that is equal to the transition between the defect's two charged states [18], and two capture cross-sections, which are related to the rate at which the defect captures free electrons (σ_n) and holes (σ_p) [20]. In this study, the values of the energy levels are defined with respect to the intrinsic energy level of Si (E_i). The recombination lifetime (τ_{SRH}) associated with those defects is described by the Shockley-Read-Hall (SRH) equation [21,22]:

$$\tau_{SRH} = \frac{\tau_{n0}(p_0 + p_1 + \Delta n) + \tau_{p0}(n_0 + n_1 + \Delta n)}{n_0 + p_0 + \Delta n}, \quad (2)$$

where τ_{p0} (τ_{n0}) is the hole (electron) lifetime parameter as defined in Eq. (3) (Eq. (4)), and p_1 (n_1) is defined in Eq. (5) (Eq. (6)).

* Corresponding author.

E-mail address: sijin.wang@student.unsw.edu.au (S. Wang).

$$\tau_{p0} = \frac{1}{\sigma_p v_p N_t}, \quad (3)$$

$$\tau_{n0} = \frac{1}{\sigma_n v_n N_t}. \quad (4)$$

where v_p (v_n) is the hole (electron) thermal velocity in Si and N_t is the defect concentration.

$$p_1 = n_i e^{\frac{E_t - E_i}{k_B T}}, \quad (5)$$

$$n_1 = n_i e^{\frac{E_t - E_i}{k_B T}}. \quad (6)$$

Two-level defects are a subcategory of multi-level defects [23]. They have three charge states and two defect recombination energies (E_{t1} and E_{t2}) [18], with E_{t1} denoting the energy transition between the most positively charged state and the middle charge state while E_{t2} represents the transition between the most negatively charged state and the middle charge state [23]. Similar to one-level defects, each defect energy is associated with two capture cross-sections ($\sigma_{n1/2}$ for electrons and $\sigma_{p1/2}$ for holes). The two-level defect lifetime is determined by the Sah-Shockley equation [24]:

$$\tau_{\text{Sah-Shockley}} = \frac{1 + \frac{\sigma_{n1} v_n n_1 + \sigma_{p1} v_p p_1 + \sigma_{p2} v_p p_2 + \sigma_{n2} v_n n_2}{\sigma_{p1} v_p p_1 + \sigma_{n1} v_n n_1} + \frac{\sigma_{n2} v_n n_2 + \sigma_{p2} v_p p_2}{\sigma_{n2} v_n n_2 + \sigma_{p2} v_p p_2}}{N_t (n_0 + p_0 + \Delta n)} \left[\left(\frac{\sigma_{n1} \sigma_{p1} v_n v_p}{\sigma_{p1} v_p p_1 + \sigma_{n1} v_n n_1} \right) + \left(\frac{\sigma_{n2} \sigma_{p2} v_n v_p}{\sigma_{n2} v_n n_2 + \sigma_{p2} v_p p_2} \right) \right], \quad (7)$$

where n_2 and p_2 are defined in Eq. (8) and Eq. (9):

$$n_2 = n_i e^{\frac{E_{t2} - E_i}{k_B T}}, \quad (8)$$

$$p_2 = n_i e^{\frac{E_{t2} - E_i}{k_B T}}. \quad (9)$$

The investigation of defects in Si is commonly performed using temperature- and injection-dependent lifetime spectroscopy (TIDLS) [25]. This technique involves lifetime measurements at different temperatures and injection levels [26]. Various analytical methods have been developed to extract the parameters of one-level defects (E_t , σ_n , σ_p) using TIDLS, including the defect parameter solution surface (DPSS) [25], the linearised DPSS [27], and the Newton-Rapson method [28]. Recently, ML-based approaches have been developed to extract these parameters as well [29–31]. However, it is difficult to distinguish

whether the recombination is dominated by two independent one-level defects or one two-level defect [23]. Furthermore, it is challenging to extract the defect parameters (E_{t1} , σ_{n1} , σ_{p1} , E_{t2} , σ_{n2} , σ_{p2}) based on TIDLS measurements [23].

This paper presents an ML-based approach that overcomes these challenges, significantly easing the parameter extraction process. The devised method can distinguish between two independent one-level defects and a two-level defect, as well as extract the parameters of a two-level defect based on TIDLS measurements.

2. Methodology

The workflow for the ML pipeline extracting defect parameters from TIDLS data is presented in Fig. 1. Initially, a **Defect Classification Model** (see below) is employed to differentiate between two one-level-defects and one two-level-defect recombination lifetimes. If the defect is classified as a one-level defect, the established ML methods of Buratti et al. [29,30] are utilised to extract the corresponding defect parameters. On the other hand, if the defect is classified as a two-level defect, the **Energy Level Classification Model** (see below) is used to assign the defect, based on its energy level, into one of four distinct sets. Subsequently, for each defect set, a **Regression Model** is developed to accurately extract the associated defect parameters, thereby completing the extraction process. Hence, the proposed framework consists of three distinct ML models, namely the Defect Type Classification Model, Energy Level Classification Model, and Regression Model.

2.1. Defect Type Classification Model

The Defect Type Classification Model identifies whether the measured lifetime is impacted by either two independent one-level defects or a two-level defect.

A dataset of more than 80,000 random combinations of defect parameters (E_{t1} , E_{t2} , σ_{n1} , σ_{p1} , σ_{n2} , σ_{p2}) within predefined ranges was simulated. This dataset was then used to generate TIDLS measurements using the Sah-Shockley or SRH equations. The resulting recombination lifetimes were computed between $1 \times 10^{13} \text{ cm}^{-3}$ and $1 \times 10^{17} \text{ cm}^{-3}$ (with 100 data points) at six different temperatures ranging from 150 K to 400 K. The simulations assume p-type wafers, n-type wafers, or both polarities with a fixed bulk doping concentration, N_{dop} . The ranges and specific values used in these simulations are detailed in Table 1.

Half of the defects were assigned as two-level defects, while the remaining half were allocated as two independent one-level defects. For

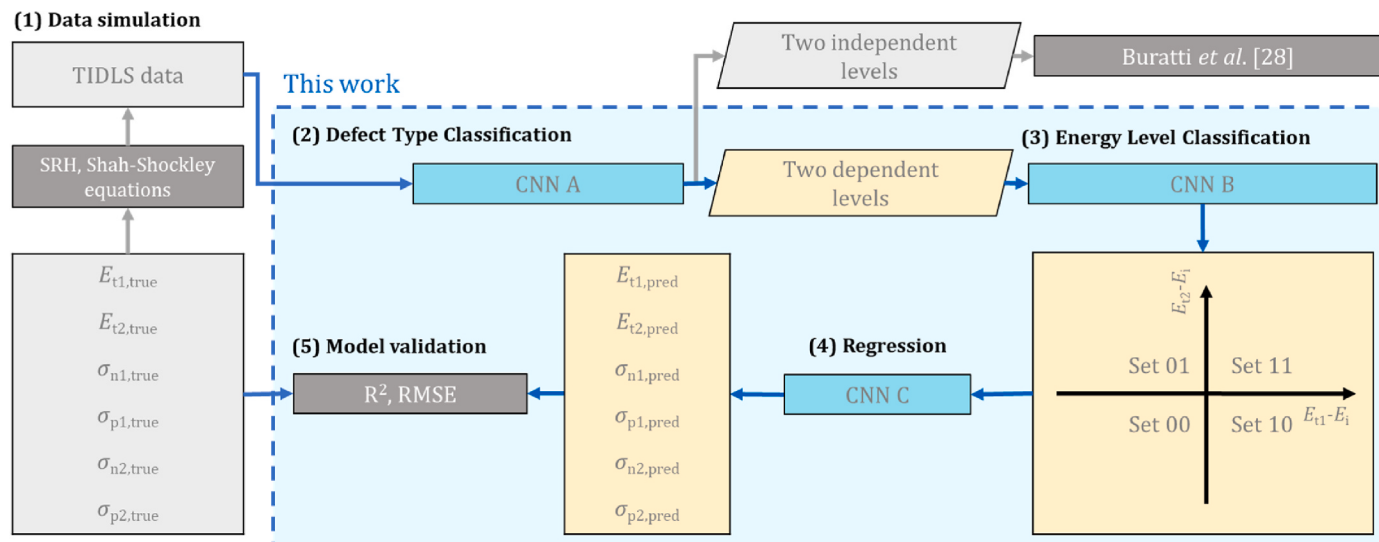


Fig. 1. The workflow of the ML pipeline.

Table 1
Simulated defect parameter ranges.

Parameter name	Symbol	Range
Defect energy level	E_{t1}, E_{t2}	-0.55 to 0.55 eV
Defect capture cross-section	$\sigma_{n1}, \sigma_{p1}, \sigma_{n2}, \sigma_{p2}$	1×10^{-13} to $1 \times 10^{-17} \text{ cm}^2$
Defect concentration	N_t	$1 \times 10^{12} \text{ cm}^{-3}$
Bulk doping concentration	N_{dop}	$1 \times 10^{15} \text{ cm}^{-3}$
Excess carrier concentration	Δn	Log scale from 1×10^{13} to $1 \times 10^{17} \text{ cm}^{-3}$
Temperature	T	150 K, 200 K, 250 K, 300 K, 350 K, 400 K

the case of two independent one-level defects, their lifetimes were computed individually using the Shockley-Read-Hall equation (τ_1 and τ_2) and then combined (τ_{com}):

$$\frac{1}{\tau_{\text{com}}} = \frac{1}{\tau_1} + \frac{1}{\tau_2} \quad (10)$$

The data was shuffled and divided into training (90 %) and testing (10 %) datasets. As the simulated lifetime data varies by several orders of magnitude, the classification model may be challenged by gradient explosion [32]. To address this challenge, the logarithm of the lifetime with base 10 (τ_{\log}) was used instead. Furthermore, τ_{\log} was scaled using a MinMax scaler [32]:

$$\tau_{\text{scaled}} = \frac{\tau_{\log} - \min(\tau_{\log})}{\max(\tau_{\log}) - \min(\tau_{\log})}, \quad (12)$$

where τ_{scaled} is the scaled lifetime and $\min/\max(\tau_{\log})$ is the minimum/maximum value of τ_{\log} .

For the defect type classification, a convolutional neural network (CNN) classifier [32] was employed, please see Appendix A for its detailed structure. During the training process, the independent variable was τ_{scaled} , while the target variable was the labelled one- or two-level defect. The performance of the model was evaluated using the accuracy and confusion matrices. Accuracy is defined as the proportion of the correct predictions over the number of total predictions [32]:

$$\text{Accuracy} = \frac{\sum_{i=1}^{i=N} 1(\hat{y}_i = y_i)}{N}, \quad (13)$$

where N is the number of samples, \hat{y}_i is the predicted value for the i^{th} sample, and y_i is the true value.

The performance of a classification model can be illustrated using a confusion matrix where the rows (columns) represent actual (predicted) values, and each entry denotes the proportion of instances of the corresponding cases [32].

2.2. Energy Level Classification Model

The Energy Level Classification Model aims to categorise two-level defects into four distinct sets based on their energy levels: both energy levels below the intrinsic energy of silicon, E_i (Set 00), both above E_i (Set 11), $E_{t1} > E_i$ and $E_{t2} < E_i$ (Set 10), and $E_{t1} < E_i$ and $E_{t2} > E_i$ (Set 01).

The reason for having the Energy Level Classification Model is the inherent complexities in determining defect energy levels in silicon photovoltaic (PV) cells. When analysing a one-level defect, there are usually two potential solutions for the defect energy level E_b , one in each half of the bandgap [25,30]; determining the true solution is challenging. This complexity is mirrored in the characterisation of two-level defects, where four possible solutions emerge, corresponding to the four defined sets above. To ascertain which set encompasses the actual solution, a distinct CNN model is employed, named the Energy Classification Model.

During simulation, more than 80,000 defect parameters were generated for each set, and their corresponding lifetime was calculated using the Sah-Shockley equation. These four categories were then combined and randomly shuffled to create a unified dataset that includes the four distinct labels.

During the training phase, τ_{scaled} were used as the input variables, while the target variable is the label of that defect (Set 11, Set 10, Set 01, Set 00). The performance evaluation was based on accuracy and the confusion matrices.

2.3. Regression model

The training and testing of the regression models were conducted independently for each set (Set 11, Set 10, Set 01, and Set 00). For each set, another 800,000 sets of defect parameters were simulated. Then, the corresponding two-level lifetime was calculated using the Sah-Shockley equation and scaled according to Eq. (12).

The regression model employed in this study is a CNN regressor [33] with two convolutional layers and two fully connected layers, the detailed structure of the CNN model is shown in Appendix A. In the training phase, τ_{scaled} was used as the input variable, while the target variables were the six defect parameters ($E_{t1}, E_{t2}, \sigma_{n1}, \sigma_{p1}, \sigma_{n2}, \sigma_{p2}$). The evaluation metrics for this task were the coefficient of determination (R^2 score) and the mean absolute error (MAE) [32], which are defined in Eq. (14) and Eq. (15):

$$R^2 = 1 - \frac{\sum_{i=0}^{N-1} (y_i - \hat{y}_i)^2}{\sum_{i=0}^{N-1} (y_i - \bar{y})^2}. \quad (14)$$

where y_i is the i^{th} value of y , \hat{y}_i is the prediction value of y_i , and \bar{y} is the average of the true values. The R^2 score provides a measure of how well the predicted and true values are aligned; a value of unity indicates a perfect prediction. A perfect prediction is also indicated by an MAE of zero:

$$\text{MAE}(y, \hat{y}) = \frac{1}{N} \sum_{i=0}^{N-1} |y_i - \hat{y}_i|. \quad (15)$$

2.4. Experimental validation

To demonstrate the effectiveness of the proposed method, samples whose lifetime is dominated by boron-oxygen (BO) defects were used. Previous studies have indicated that the defects associated with BO have two energy levels [23,34].

Both p-type (boron-doped Czochralski (Cz), $N_{\text{dop}} = 8.5 \times 10^{14} \text{ cm}^{-3}$) and n-type (boron and phosphorus co-doped Cz, $N_{\text{dop}} = 2.0 \times 10^{15} \text{ cm}^{-3}$) wafers were used. For the preparation process, see Appendix B and Ref. [23]. Their effective lifetime was measured at four temperatures: 223 K, 263 K, 303 K, and 343 K. Before the measurements, the BO defects were activated by one sun equivalent illumination (using halogen lamps) for five days [23]. The effective lifetime after this light soaking process is labelled as τ_{LS} . Then, the defects were deactivated via annealing at 200 °C in the dark for 30 min [23]. The effective lifetime after this process is labelled as τ_{DA} . The defect recombination lifetime (τ_{defect}) was calculated as:

$$\frac{1}{\tau_{\text{defect}}} = \frac{1}{\tau_{\text{LS}}} - \frac{1}{\tau_{\text{DA}}}. \quad (16)$$

After extracting the τ_{defect} , the lifetime data was smoothed using a Savitzky-Golay filter [35] with 30 window lengths and an order of two. The Savitzky-Golay filter was selected due to its flexibility in tuning the window length and the polynomial order to ensure smoothing while still preserving the key features of the original data [35]. The lifetime data points were extracted within the range from $1 \times 10^{14} \text{ cm}^{-3}$ to $3.17 \times$

10^{16} cm^{-3} and the ML models were used for the analysis.

3. Results

3.1. Tested on simulated data

The ML models underwent rigorous testing with simulated data to verify their capability in accurately learning the Sah-Shockley equation. The parameters for the simulated data are meticulously detailed in Table 1. Following a random partition, 90 % of the dataset was designated for training, while the remaining 10 % was set aside for testing. The focus of the subsequent analyses is on the validation results derived from this 10 % testing set.

3.1.1. Defect Type Classification Model

The Defect Type Classification Model aims to distinguish between the cases of two independent one-level defects and two-level defects.

Table 2 presents the confusion matrix of the results obtained using the p-type wafers. The model achieved an impressive accuracy of 88 %. To our knowledge, besides the method of Zhu et al. [23], there are no other methods that can distinguish between two independent one-level defects and two-level defects. Since no curve-fitting process is required, the ML-based method offers a simpler approach to address this task.

The few misclassifications can be attributed to cases where the recombination lifetime by the two-level defect lifetime is similar to one defect energy level alone. For instance, based on the Sah-Shockley statistics, when both E_{t1} and E_{t2} are near the conduction band, the recombination through E_{t1} is predominant. Consequently, the resulting lifetime is primarily sensitive to E_{t1} , σ_{n1} , and σ_{p1} , with the impact of the remaining three parameters being negligible. Hence, the two-level defect behaves similarly to a one-level defect, posing a significant challenge for the model to distinguish between the two cases. An illustration of this scenario is shown in Fig. C-1 (a) in Appendix C, where the lifetimes of a one-level defect ($E_t = 0.5 \text{ eV}$) are almost identical to two-level defects with $E_{t1} = 0.5 \text{ eV}$ and $E_{t2} = 0.51 \text{ eV}$.

Misclassification can also occur when there is a significant difference in the capture cross-sections between E_{t1} and E_{t2} . Specifically, when the capture cross-section of one defect/level is much larger than that of the other defect/level, the recombination of the defect with the larger capture cross-section dominates, rendering the impact of the other defect negligible. Hence, the lifetime behaviour of the two independent defects resembles that of a one-level defect; Fig. C-1 (b) in Appendix C illustrates this scenario. One approach to further improve the model's accuracy is to generate additional data within this ambiguous region, thereby enhancing the model's training for these challenging cases.

The results for the n-type wafers are similar with an accuracy of 89 % (see Appendix D). However, if wafers with both polarities are available for defect lifetime, the Defect Type Classification Model can reach a higher accuracy of 92 % (Appendix D).

3.1.2. Energy Level Classification Model

As discussed in Section 3.2, the Energy Level Classification Model is an important precursor to the regression analysis. It categorises the defects into four groups based on their E_{t1} and E_{t2} . After this categorisation, the regression model extracts the defect parameters of the two-level defects separately.

Table 3 displays the corresponding confusion matrix. The overall

Table 2
The confusion matrix of the Defect Type Classification Model (p-type wafers).

True	Pred
One two-level	Two one-level
One two-level	47.6 %
Two one-level	7.8 %
	42.4 %

Table 3

Confusion matrix of the Energy Level Classification Model (p-type wafers).

	Set 11	Set 10	Set 01	Set 00	Specificity
Set 11	19.1 %	2.8 %	2.8 %	0.3 %	76.4 %
Set 10	4.8 %	18.4 %	0.4 %	1.4 %	73.6 %
Set 01	3.5 %	0.4 %	17.6 %	3.5 %	70.4 %
Set 00	0.7 %	1.8 %	4.3 %	18.2 %	72.8 %

accuracy for this classification model using the lifetime obtained using p-type wafers is 73.3 %, which indicates a solid foundation for the subsequent parameter extraction step.

The misclassifications could be attributed to the minimal change observed in the lifetime curve when one of the defect energies approaches zero (the intrinsic Fermi energy of Si). Fig. C-2 illustrates this challenge by plotting the lifetime when E_{t1} is fixed at 0.4 eV and E_{t2} is varied between -0.1 eV and 0.1 eV . In this case, the lifetime curve remains almost unaffected (within the range of about 1 ns), reducing the accuracy of the model in classifying the defect as Set 10 ($E_{t2} < 0$) or Set 11 ($E_{t2} > 0$). To further improve energy level classification accuracy, lifetime measurements of both n-type and p-type wafers can be utilised, C discussed in the next session.

The classification results for the n-type wafer are similar with an accuracy of 72 % (see Appendix D) while if wafers with both polarities are available for lifetime measurements, the Energy Level Classification Model can reach a higher accuracy of 84.4 % (Appendix D).

3.1.3. Regression model

The regression analysis is conducted individually for each of the sets (Set 11, Set 10, Set 01, and Set 00). The predicted defect parameters are then combined into one figure. The predicted versus true values of the six defect parameters are presented in Fig. 2. The ML-based models demonstrate high accuracy in solving this challenging problem, achieving an R^2 score above 0.9 for both defect energy levels on the test set. In this study, the capture cross-sections are predicted. While it is impossible in practice to predict the absolute value of the capture cross sections without knowing the defect density, the developed ML model can effectively predict the product $N_t \times \sigma$.

It is observed that the ML models predict the defect parameters associated with the most positively charged state ($E_{t1}, \sigma_{n1}, \sigma_{p1}$) more accurately compared to the negative state parameters ($E_{t2}, \sigma_{n2}, \sigma_{p2}$). This can be shown by R^2 for $E_{t1}, \sigma_{n1}, \sigma_{p1}$ being higher compared to $E_{t2}, \sigma_{n2}, \sigma_{p2}$ and the MAE for $E_{t1}, \sigma_{n1}, \sigma_{p1}$ being lower compared to $E_{t2}, \sigma_{n2}, \sigma_{p2}$. Since in p-type semiconductors, the number of holes significantly outweighs the number of electrons, especially when the injection level is low, more defects capture holes and therefore are in the most positively charged state. Therefore, the majority of recombination events occur through the transition between the most positively charged state and the medium charged state, which is influenced by E_{t1}, σ_{n1} , and σ_{p1} . Consequently, the defect recombination lifetime in p-type Si is more sensitive to $E_{t1}, \sigma_{n1}, \sigma_{p1}$ than to $E_{t2}, \sigma_{n2}, \sigma_{p2}$. This is demonstrated in Fig. C-3, where the defect lifetime measured on p-type wafers remains almost unchanged when E_{t1} is kept fixed at 0.5 eV while E_{t2} is varied from 0.45 eV to 0.55 eV. In contrast, there is a significant change in the defect lifetime when E_{t1} is varied from 0.45 eV to 0.55 eV while E_{t2} is kept constant at 0.5 eV.

In n-type Si, the opposite behaviour occurred where the ML model predicts $E_{t2}, \sigma_{n2}, \sigma_{p2}$ more accurately than $E_{t1}, \sigma_{n1}, \sigma_{p1}$ (see Appendix D).

Note that the developed model is also capable of predicting the capture cross-section ratios; the results are shown in Appendix E.

To improve the prediction, it is recommended to measure the defect lifetime of the same defect using both p- and n-type wafers. In this case, the ML model accesses a richer dataset where the lifetime is sensitive to the changes in all the six defect parameters. This is demonstrated in Fig. 3 where predicated vs true plots are shown for this case (p- and n-type wafers). After using both polarities, while the R^2 score for E_{t1} , the

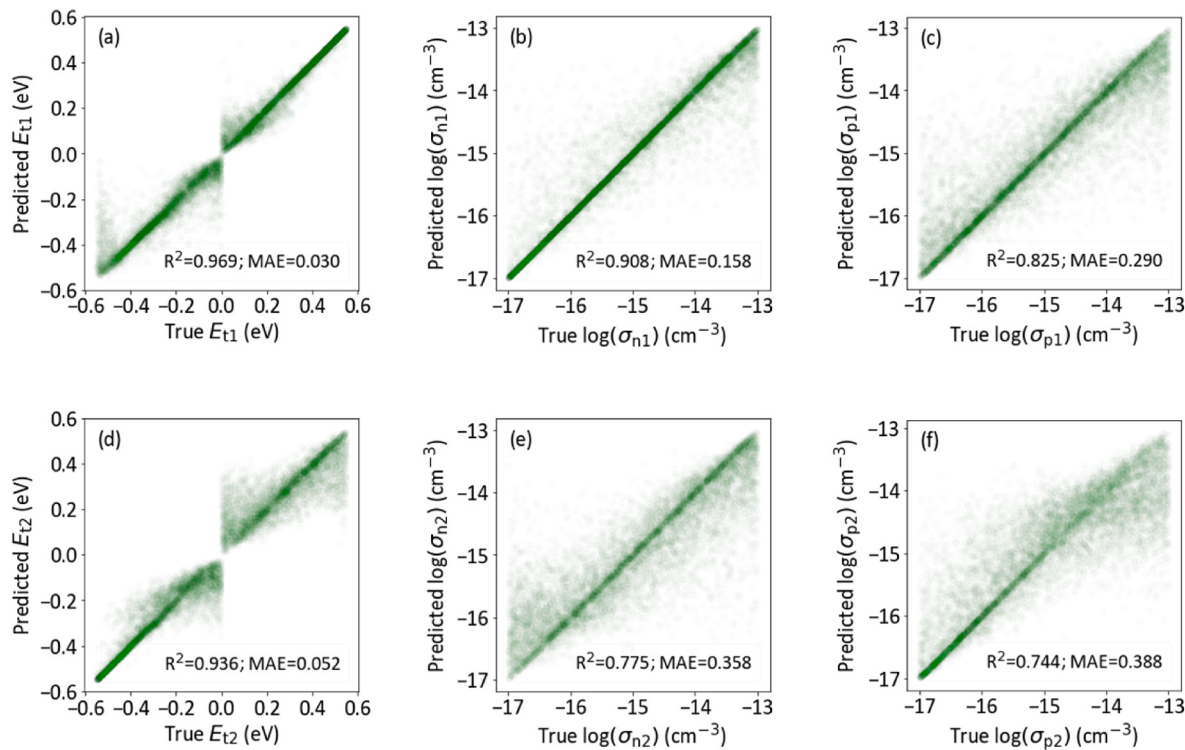


Fig. 2. Predicted vs true plots for the regression models, using the data parameters indicated in Table 1 (p-type wafers).

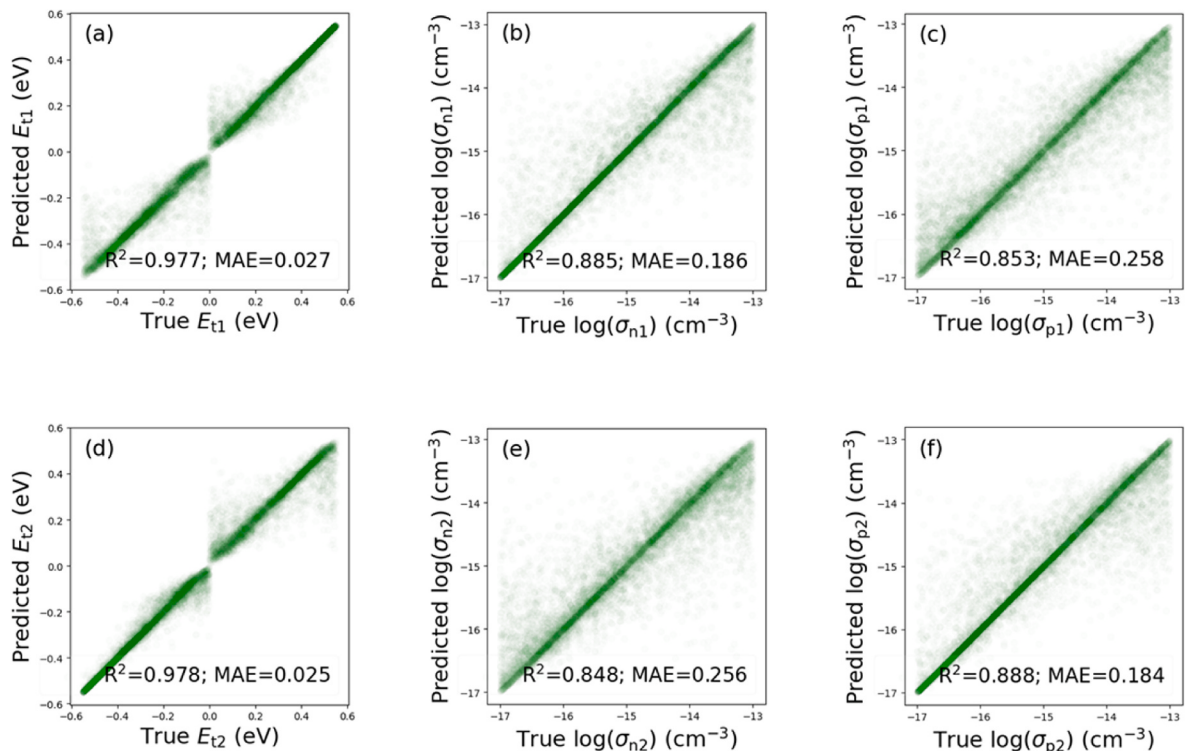


Fig. 3. Predicted vs true plots for the regression models, using the data parameters indicated in Table 1 (p- and n-type wafers).

log of σ_{n1} , and σ_{p1} are similar compared to using a p-type wafer only, the R^2 score for the other three defect parameters improved significantly. Specifically, the R^2 score for E_{t2} increased from 0.936 to 0.978, and the R^2 score of the log of σ_{n1} , and σ_{p1} increased by approximately 0.1 as well. The comparison between Figs. 2 and 3 shows that using the defect lifetime in both polarities can improve ML prediction accuracy.

3.2. Experimental data

To validate the proposed method, the measured lifetimes of BO-related defects, which are known as two-level defects [23,34], were analysed using the ML models.

The Defect Type Classification Model successfully identified the defect as a two-level defect while the Energy Level Classification Model identified it as Set 10. The Regression Model determined the energy levels to be $E_{t1} = 0.153$ eV and $E_{t2} = -0.288$ eV.

Fig. 4 marks the obtained ML predictions and the reported parameters by two previous studies. The BO energy levels extracted by Nieuwelt et al. [34] are marked by a red star whereas the background is the residual map calculated by Zhu et al. [23] where the dark area indicates a low-fitting residual, which should include the correct solution.

As can be seen, the ML prediction using both the p- and n-type wafers agrees well with the results by Nieuwelt et al. [34] (close to the red star) and Zhu et al. [23] (falls inside the low residual region). The parameters obtained using only one of the polarities fall outside the region determined by Zhu and are further away from the red star. The prediction using only a p-type wafer estimated E_{t1} close to the value obtained from Nieuwelt et al. [34]. However, the E_{t2} prediction using only the p-type lifetime falls outside the dark region and was far away from the literature value [34]. This means that the ML-predicted E_{t2} using only the p-type wafer is less accurate compared to E_{t1} . On the other hand, the prediction using only the n-type wafer aligns well with the literature value [34] on the E_{t2} axis but has a larger error predicting E_{t1} . Finally, when using the defect lifetime of both polarities, the predictions for both defect energy levels are the most accurate.

One bottleneck of the developed ML-based model is its reliance on lifetime measurements at specific temperatures. This inflexibility poses challenges when measurements at certain temperatures are unavailable. A potential method to mitigate this issue, and a subject for future research, is to train the model to calculate parameters even in the absence of some temperature-specific lifetime measurements. The model would dynamically adjust the error range based on available data, utilising versions tailored to various measurement conditions. Each model would be trained to handle different scenarios of missing data, allowing for the selection of the most appropriate model based on the actual measurement conditions.

Future research will focus on extending the developed method to investigate multi-level defects. The ultimate aim is to develop a pipeline that identifies the dominant defects, classifies them, and extracts their parameters regardless of the number of energy levels. Additionally, it would be advantageous to add a capability that suggests ways to reduce the uncertainty associated with the analysis, such as by measuring lifetime over additional temperature or injection ranges.

4. Conclusion

In conclusion, this study presented a novel ML-based approach that solves two challenging problems in the field of lifetime spectroscopy. The first challenge involves accurately distinguishing between the lifetime of two-level defects and two independent single-level defects. If the defect is a two-level defect, the second challenge focuses on extracting the defect parameters using TIDLS.

To address these challenges, this study proposes a pipeline comprising three ML models. Firstly, the proposed Defect Type Classification Model distinguishes the lifetime of two-level defects and two independent one-level defects with an accuracy of 93 %. Secondly, if the

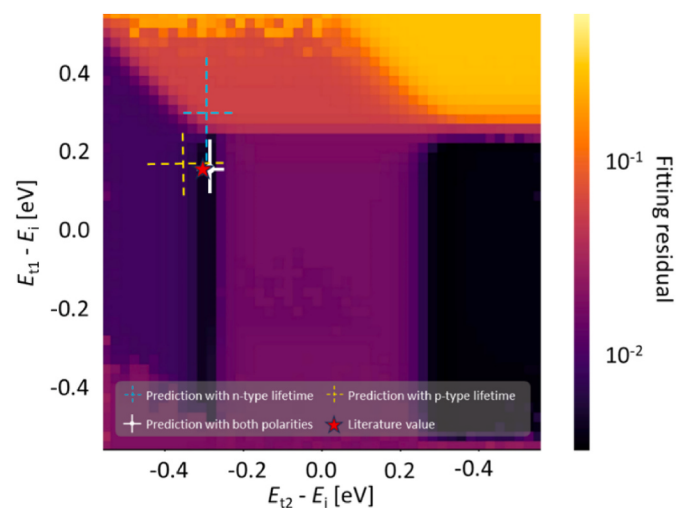


Fig. 4. A comparison between ML predictions, residual map of Zhu et al. [23], and the results by Nieuwelt et al. [34] marked as a red star.

defect is two-level, another Energy Level Classification Model is built to further classify the defect into four different subsets. Finally, a regression model is trained and tested on each subset. If the defect lifetime is measured in both p-type and n-type semiconductors, the developed model can predict the defect energy levels with an R^2 above 0.95 and the capture cross-sections with $R^2 > 0.8$. A BO-related defect was used as an experimental validation: The ML model successfully identified the BO as a two-level defect and determined defect energy levels within 0.03 eV from previous studies.

The developed capabilities are capable to unlock the full potential of lifetime measurements and assist with the development of strategies for the improvements of Si wafer quality. Furthermore, the results show that the prediction accuracy for the ML models is higher when the defect lifetime in both n-type and p-type wafers is available compared to only having one polarity.

CRediT authorship contribution statement

Sijin Wang: Writing – review & editing, Writing – original draft, Visualization, Validation, Software, Methodology, Investigation, Formal analysis, Data curation, Conceptualization. **Brendan Wright:** Writing – review & editing, Software, Methodology, Formal analysis. **Yan Zhu:** Writing – review & editing, Validation, Methodology, Investigation, Formal analysis. **Yoann Buratti:** Data curation. **Ziv Hameiri:** Writing – review & editing, Supervision, Resources, Project administration, Methodology, Funding acquisition, Formal analysis, Conceptualization.

Declaration of generative AI and AI-assisted technologies in the writing process

During the preparation of this paper, the authors used ChatGPT to check the grammar. After using this tool/service, the authors reviewed and edited the content as needed; they take full responsibility for the content of the publication.

Declaration of competing interest

The authors declare that they have no known competing financial interests or personal relationships that could have appeared to influence the work reported in this paper.

Data availability

Data will be made available on request.

Acknowledgement

This work was supported by the Australian Government through the Australian Renewable Energy Agency (ARENA, Grant 2022/TRAC002).

Appendix A. The CNN structure

The CNN models used in this study consist of two 1D convolutional layers and two fully connected layers. The first convolutional layer has a kernel size of three, a padding size of one, and an output channel number of eight. The second convolutional layer has a kernel size of three, a padding size of one, and an output channel size of sixteen. After that, the data is flattened and goes through two fully connected layers. The first fully connected layers have 512 nodes, and the second fully connected layer has 128 notes.

The output size is one for the Defect Classification model since it is a binary classification. The output size is two for the Energy Level Classification model, one indicating whether E_{t1} is above or below the intrinsic energy level, the other indicating whether E_{t2} is above or below the intrinsic energy level. Finally, the output size is six for the Regression model, one for each of the defect parameters.

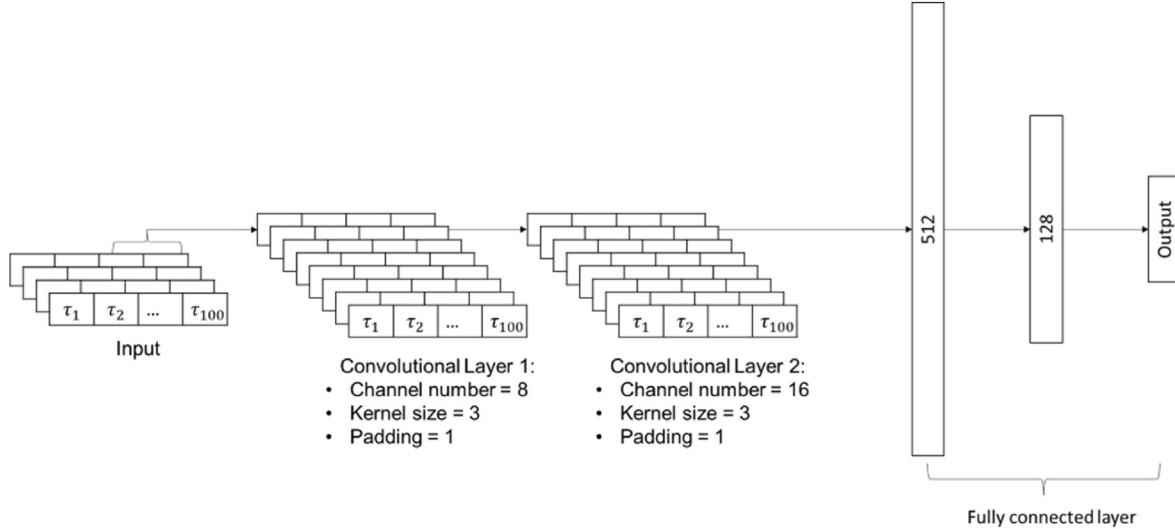


Fig. A-1. The CNN structure of the ML models.

Appendix B. Sample preparation

After doping, the oxygen content was measured using Fourier Transform Infrared Spectroscopy (FTIR) by the ASTM F1188 standard [36], the oxygen content was measured to be 13.6 parts per million atoms (ppma) for the p-type wafer and 17.6 ppma for the n-type wafer. To decrease the presence of metallic contaminants, both wafers were subjected to a gettering process using phosphorus at a temperature of 785 °C for a duration of half an hour. Post-gettering, the samples underwent a dip in hydrogen fluoride (HF) to achieve a hydrophobic surface and were then etched in tetramethylammonium hydroxide (TMAH) for 6 min to remove the heavily doped layers.

During the passivation process, the p-type wafer underwent passivation through the application of a 20 nm thick aluminium oxide (AlOx) layer, which was deposited using atomic layer deposition (ALD) at a temperature of 175 °C. This layer was activated by a forming gas anneal at 425 °C for 30 min. A 70 nm Si nitride (SiNx) film was used to passivate the compensated n-type wafer, deposited at 300 °C through plasma-enhanced chemical vapour deposition (PECVD).

Appendix C. Prediction errors explanation

Fig. C-1 is an example of a case where the Defect Classification Model have difficulty distinguishing between a two-level defect and two independent one-level defects.

Fig. C-1 (a) shows an example of both E_{t1} and E_{t2} being close to the conduction band, which makes the two-level defect lifetime close to the one-level defect. Therefore, according to Eq. (5) and Eq. (6), when $E_{t1} - E_i$ is large, n_1 is much larger than p_1 . According to Eq. (8) and Eq. (9), a large $E_{t2} - E_i$ lead to n_2 much larger than p_2 . Therefore, the parameters related to E_{t1} σ_1 , and σ_1 dominate in the Sah Shockley equation. As a result, the defect lifetime is very similar to a one-level defect with only E_{t1} and its capture cross-sections. The mathematical derivation is shown below:

$$\begin{aligned} \tau_{\text{Sah-Shockley}} &= \frac{1 + \frac{\sigma_{n1}v_n n_1 + \sigma_{p1}v_p p_1}{\sigma_{p1}v_p p_1 + \sigma_{n1}v_n n} + \frac{\sigma_{p2}v_p p_2 + \sigma_{n2}v_n n}{\sigma_{n2}v_n n_2 + \sigma_{p2}v_p p}}{N_t(n_0 + p_0 + \Delta n) \left[\left(\frac{\sigma_{n1}\sigma_{p1}v_n v_p}{\sigma_{p1}v_p p_1 + \sigma_{n1}v_n n} \right) + \left(\frac{\sigma_{n2}\sigma_{p2}v_n v_p}{\sigma_{n2}v_n n_2 + \sigma_{p2}v_p p} \right) \right]} \approx \frac{1 + \frac{\sigma_{n1}v_n n_1 + \sigma_{p1}v_p p_1}{\sigma_{p1}v_p p_1 + \sigma_{n1}v_n n}}{N_t(n_0 + p_0 + \Delta n) \left[\left(\frac{\sigma_{n1}\sigma_{p1}v_n v_p}{\sigma_{p1}v_p p_1 + \sigma_{n1}v_n n} \right) \right]} \\ &= \frac{\sigma_{p1}v_p p_1 + \sigma_{n1}v_n n + \sigma_{n1}v_n n_1 + \sigma_{p1}v_p p}{N_t(n_0 + p_0 + \Delta n) (\sigma_{n1}\sigma_{p1}v_n v_p)} = \frac{\frac{1}{\sigma_p v_p N_t} (p_0 + p_1 + \Delta n) + \frac{1}{\sigma_n v_n N_t} (n_0 + n_1 + \Delta n)}{n_0 + p_0 + \Delta n} = \frac{\tau_{n0}(p_0 + p_1 + \Delta n) + \tau_{p0}(n_0 + n_1 + \Delta n)}{n_0 + p_0 + \Delta n} = \tau_{\text{SRH}}(E_{t1}) \end{aligned}$$

Fig. C-1 (b) shows an example of the capture cross sections related to one energy level being much larger than the other. In the plot, the capture cross-sections of E_{t1} are much larger than E_{t2} . Therefore, the recombination rate at E_{t1} is much larger than E_{t2} , which effectively dominates the recombination dynamics. As a result, the two-level lifetime is almost like having only one recombination energy E_{t1} .

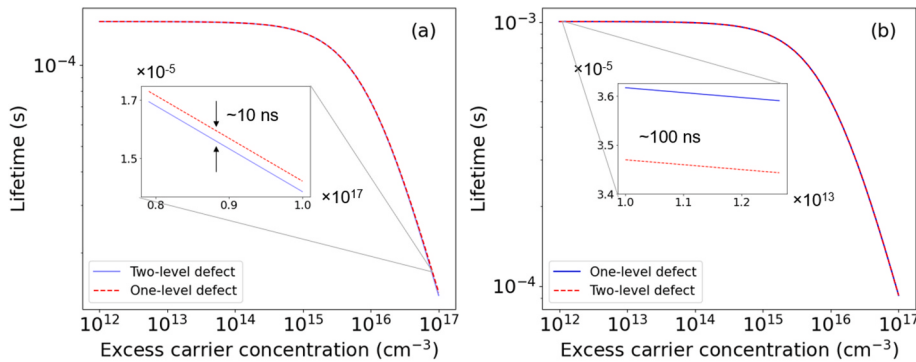


Fig. C-1. (a) Lifetime curves of two-level ($E_{t1} = 0.5 \text{ eV}$ and $E_{t2} = 0.51 \text{ eV}$) and one-level ($E_t = 0.5 \text{ eV}$) defects. The used capture cross-sections are $\sigma_{n1} = \sigma_{p1} = \sigma_{n2} = \sigma_{p2} = 1 \times 10^{-13} \text{ cm}^2$, while $N_t = 10^{12} \text{ cm}^{-3}$ and $N_{\text{dop}} = 10^{15} \text{ cm}^{-3}$, using the defect lifetime in p-type wafer. (b) The effective lifetime of two independent defects and the lifetime with one level defect ($E_t = E_{t1}$), $E_{t1} = 0.55 \text{ eV}$, $E_{t2} = 0.5 \text{ eV}$, $\sigma_{n1} = \sigma_{p1} = 10^{-13} \text{ cm}^2$, and $\sigma_{n2} = \sigma_{p2} = 10^{-17} \text{ cm}^2$, while $N_t = 10^{12} \text{ cm}^{-3}$ and $N_{\text{dop}} = 10^{15} \text{ cm}^{-3}$, using the defect lifetime in p-type wafer.

Fig. C-2 demonstrates the case where the Energy Level Classification Model struggles to distinguish between Set 11 and Set 10 when the energy values are situated at the boundary between these two categories. In this example, when $E_{t1}-E_t$ is kept constant at 0.4 eV, and $E_{t2}-E_t$ varies from -0.1 eV to 0.1 eV, the recombination is almost unchanged, making it difficult for the ML model to distinguish between Set 11 and Set 10.

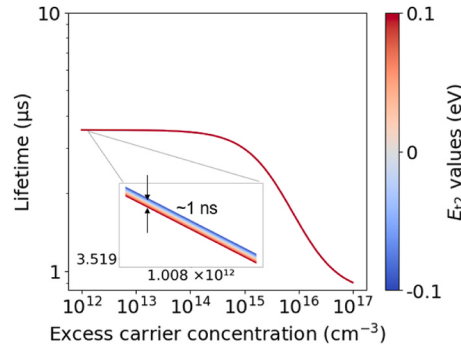


Fig. C-2. The lifetime of two-level defects where $E_{t1} = 0.4 \text{ eV}$ and E_{t2} is varied from -0.1 eV to 0.1 eV. Other parameters: $\sigma_{n1} = \sigma_{p1} = 10^{-13} \text{ cm}^2$, and $\sigma_{n1} = \sigma_{p1} = 10^{-13} \text{ cm}^2$, $N_t = 10^{12} \text{ cm}^{-3}$, and $N_{\text{dop}} = 10^{15} \text{ cm}^{-3}$, using the defect lifetime in p-type wafer.

Fig. C-3 shows the case when the Regression Model struggles to predict E_{t2} because of the low sensitivity of the Sah-Shockley equation on E_{t2} compared to E_{t1} . When E_{t1} varies, the lifetime changes significantly, but when E_{t2} varies, the lifetime is almost unchanged. This demonstrates the case when the lifetime curve is more sensitive to E_{t1} than E_{t2} .

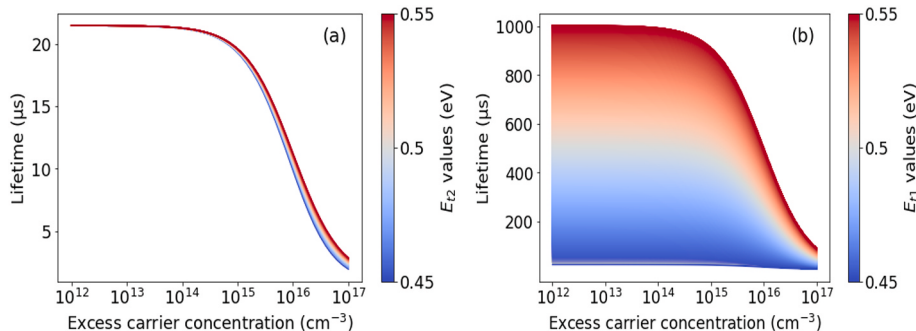


Fig. C-3. (a) The lifetime of defects with $E_{t1} = 0.5 \text{ eV}$ and E_{t2} from 0.45 eV to 0.55 eV; and (b) the lifetime of defects with E_{t1} from 0.45 eV to 0.55 eV and $E_{t2} = 0.5 \text{ eV}$. Other parameters: $\sigma_{n1} = \sigma_{p1} = \sigma_{n2} = \sigma_{p2} = 10^{-13} \text{ cm}^2$, $N_t = 10^{12} \text{ cm}^{-3}$, and $N_{\text{dop}} = 10^{15} \text{ cm}^{-3}$, using the defect lifetime using p-type wafer.

Appendix D. ML results using different polarities

Table D-1 shows the confusion matrix of the Defect Type Classification Model trained and tested on the n-type wafer. The accuracy is 89.9 %. The overall accuracy of using an n-type wafer is very similar to the p-type wafer. The most common misclassification is to misidentify two-level defects into a combination of two independent one-level defects.

Table D-1

The confusion matrix of the Defect Type Classification Model using the defect lifetime in the n-type wafer.

Pred True	One two-level	Two one-level
One two-level	47.3 %	2.7 %
Two one-level	7.4 %	42.6 %

Table D-2 shows the confusion matrix of the Defect Type Classification Model results trained and tested on the defect lifetime obtained using both p-type and n-type wafers. The accuracy is 92 %; higher than using only n-type or p-type data. The most significant reduction in misclassification is to misidentify two one-level defects into one two-level defects.

Table D-2

The confusion matrix of the Defect Type Classification Model using the defect lifetime in both n-type and p-type wafers.

Pred True	One two-level	Two one-level
One two-level	45.4 %	4.6 %
Two one-level	3.4 %	46.6 %

Table D-3 shows the confusion matrix of the Energy Level Classification Model results trained and tested on the n-type wafer. The accuracy is 71.9 %, which is similar to the p-type.

Table D-3

Confusion matrix of the Energy Level Classification Model using the defect lifetime in the n-type wafer.

	Set 11	Set 10	Set 01	Set 00	Specificity
Set 11	16.9 %	5.3 %	2.1 %	0.7 %	67.6 %
Set 10	4.3 %	16.1 %	0.5 %	4.1 %	64.4 %
Set 01	1.6 %	0.4 %	20.0 %	3.0 %	80.0 %
Set 00	0.4 %	2.6 %	3.1 %	18.9 %	75.6 %

Table D-4 shows the confusion matrix of the Energy Level Classification Model results trained and tested on the lifetime in both n-type and p-type semiconductors. The accuracy is 84.4 %, which is significantly higher than using either n-type or p-type data.

Table D-4

Confusion matrix of the Energy Level Classification Model using the defect lifetime in both p-type and n-type wafers.

	Set 11	Set 10	Set 01	Set 00	Specificity
Set 11	20.1 %	2.6 %	2.0 %	0.3 %	80.4 %
Set 10	1.6 %	21.3 %	0.0 %	2.1 %	85.2 %
Set 01	1.0 %	0.1 %	22.4 %	1.5 %	89.6 %
Set 00	0.0 %	3.0 %	1.4 %	20.6 %	82.4 %

As discussed in Section 4.1.3, the ML Regression model predicts E_{t1} and its capture cross-sections better than E_{t2} and its capture cross-sections better in p-type wafers. In n-type silicon, an inverse pattern is observed: the model predicts the parameters E_{t2} , σ_{n2} and σ_{p2} more accurately compared to the other three.

Fig. D-1 shows the ML prediction accuracy for the n-type Si wafer. As a result, only using the n-type lifetime data, the ML can predict both energy levels with a correlation coefficient (R^2 score) above 0.9. The R^2 score for E_{t2} (0.973) is higher than E_{t1} (0.938), which agrees with the expectation. A similar trend happens for the capture cross-sections since the ML models can predict the capture cross-sections σ_{n2} and σ_{p2} with higher precision compared to the other two. This is because, in n-type silicon, there are more electrons than holes. Therefore, more defects are in the most negatively charged states, particularly when the injection level is low. Thus, there is more defect recombination via the transition between the medium-charged state and the most negatively charged state which is associated with E_{t2} and its capture cross-sections.

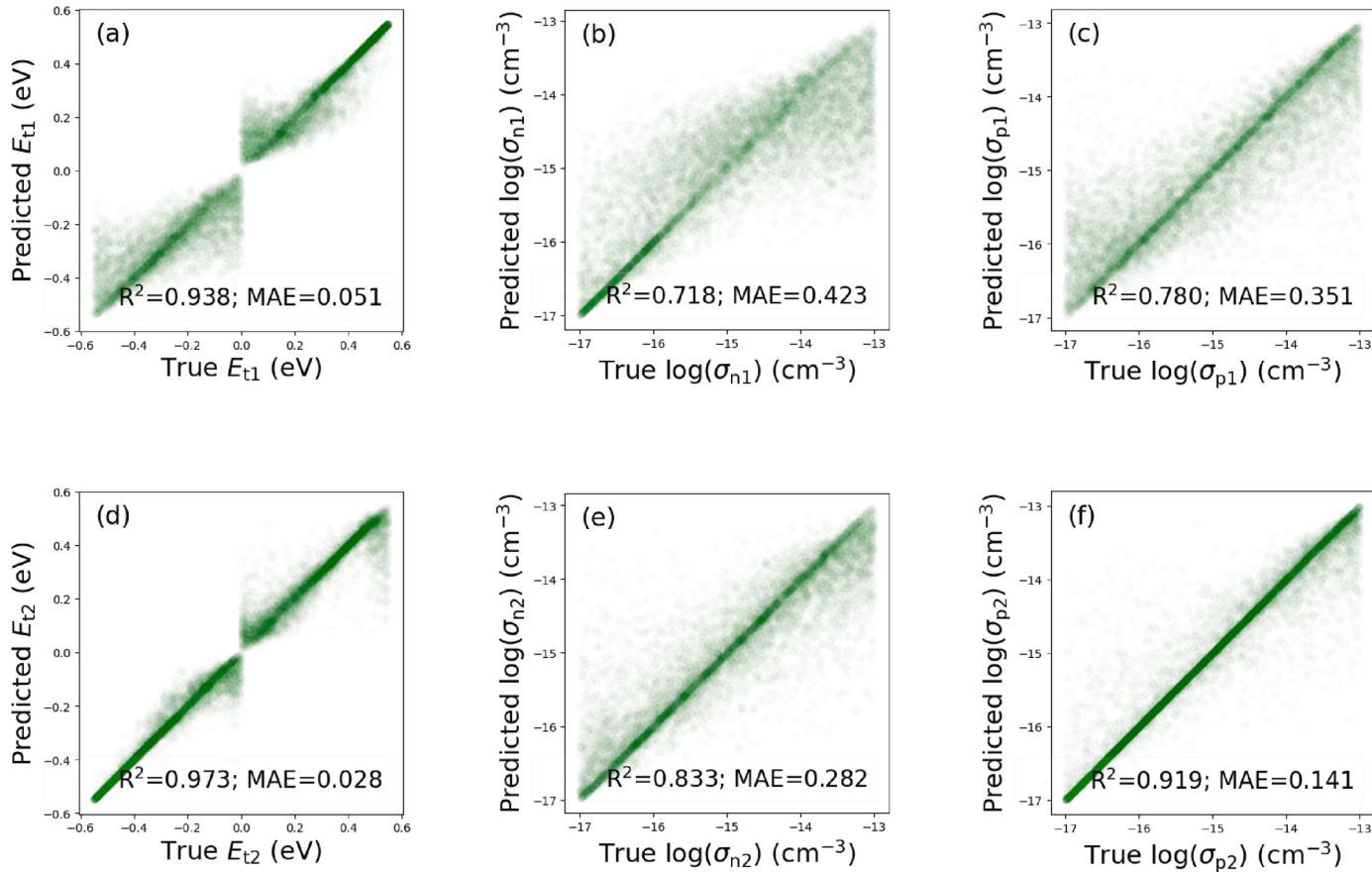


Fig. D-1. The regression results using the data parameters shown in Table 1, using the defect lifetime in the n-type wafer.

Appendix E. Capture cross-section ratio predictions

It is also very common to predict the capture cross-section ratios instead of capture cross-sections [18]. The capture cross-section ratios are defined in Eq. (17) and Eq. (18),

$$k_1 = \frac{\sigma_{n1}}{\sigma_{p1}}, \quad (17)$$

$$k_2 = \frac{\sigma_{n2}}{\sigma_{p2}}. \quad (18)$$

The proposed ML pipeline is also capable of predicting the energy levels and the ratios of the capture cross-sections, and the results are shown in Fig. E-1.

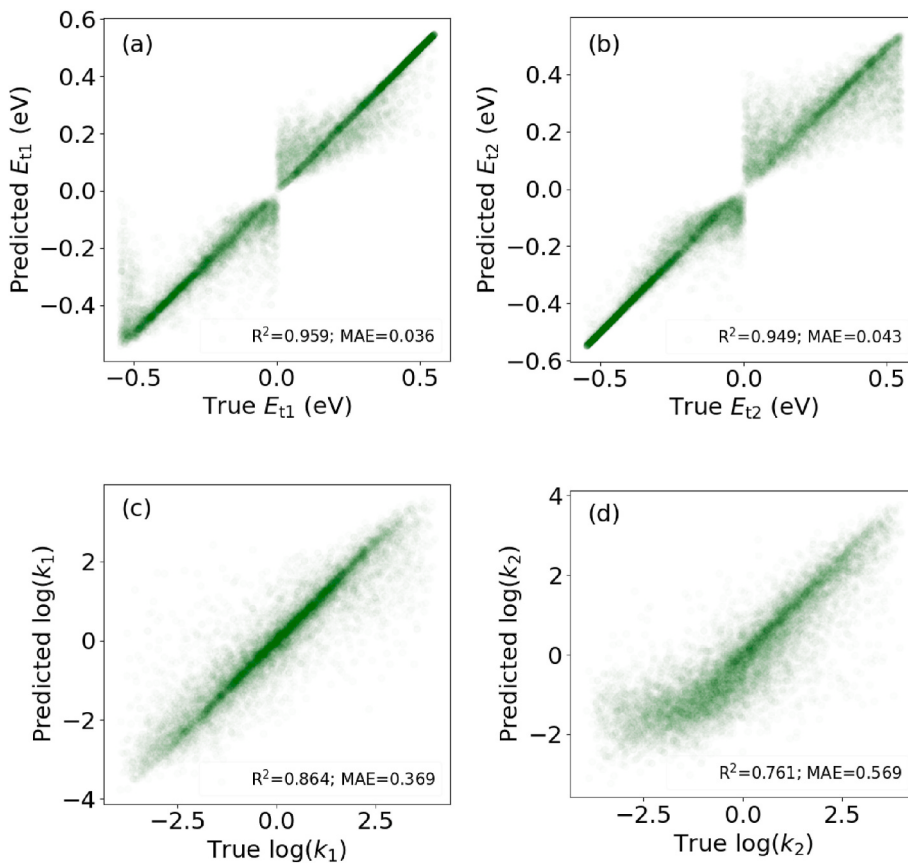


Fig. E-1. The regression results using the same data parameter indicated in Table 1, using the defect lifetime in the p-type wafer.

References

- [1] B. Lloyd, A.S. Forest, The transition to renewables: can PV provide an answer to the peak oil and climate change challenges, *Energy Pol.* 38 (11) (2010) 7378–7394, <https://doi.org/10.1016/j.enpol.2010.08.014>.
- [2] J. Zhang, Solar PV market research and industry competition report, *Earth Environ. Sci.* 632 (3) (2021) 032047, <https://doi.org/10.1088/1755-1315/632/3/032047>.
- [3] E. Mayfield, J. Jenkins, Influence of high road labour policies and practices on renewable energy costs, decarbonization pathways, and labour outcomes, *Environ. Res. Lett.* 16 (12) (2021) 124012, <https://doi.org/10.1088/1748-9326/ac34ba>.
- [4] J. Schmidt, et al., Impurity-related limitations of next-generation industrial silicon solar cells, *IEEE J. Photovoltaics* 3 (1) (2013) 114–118, <https://doi.org/10.1109/JPHOTOV.2012.2210030>.
- [5] M. Yamaguchi, K.-H. Lee, K. Araki, N. Kojima, Y. Ohshita, Analysis for efficiency potential of crystalline Si solar cells, *JMR (J. Mol. Recognit.)* 33 (17) (2018) 2621–2626, <https://doi.org/10.1557/jmr.2018.262>.
- [6] R. Basnet, et al., Understanding the strong apparent injection dependence of carrier lifetimes in doped polycrystalline silicon passivated wafers, *Sol. RRL* 8 (12) (2024) 2400087, <https://doi.org/10.1002/solr.202400087>.
- [7] T.T. Le, et al., Reassessing Iron–Gallium recombination activity in silicon, *J. Appl. Phys.* 135 (13) (2024) 133107, <https://doi.org/10.1063/5.0198737>.
- [8] A. Cuevas, D. Macdonald, Measuring and interpreting the lifetime of silicon wafers, *Sol. Energy* 76 (1) (2004) 255–262, <https://doi.org/10.1016/j.solener.2003.07.033>.
- [9] R.A. Sinton, A. Cuevas, M. Stuckings, Quasi-steady-state photoconductance, a new method for solar cell material and device characterization, in: 25th IEEE Photovoltaic Specialists Conference, 1996, pp. 457–460, <https://doi.org/10.1109/PVSC.1996.564042>.
- [10] M.A. Green, in: *Solar Cells: Operating Principles, Technology and System Applications*, first ed., UNSW, Sydney, Australia, 1992.
- [11] G.M.N. Javier, P. Dwivedi, Y. Buratti, I. Perez-Wurfl, T. Trupke, Z. Hameiri, Improvements and gaps in the empirical expressions for the fill factor of modern industrial solar cells, *Sol. Energy Mater. Sol. Cells* 253 (2023) 112183, <https://doi.org/10.1016/j.solmat.2023.112183>.
- [12] M.A. Green, Accurate expressions for solar cell fill factors including series and shunt resistances, *J. Appl. Phys.* 108 (8) (2016), <https://doi.org/10.1063/1.4942660>.
- [13] J. Schmidt, et al., Advances in the surface passivation of silicon solar cells, *Energy Proc.* 15 (2012) 30–39, <https://doi.org/10.1016/j.egypro.2012.02.004>.
- [14] D. Yan, et al., Silicon solar cells with passivating contacts: classification and performance, *Prog Photovolt* 31 (4) (2023) 310–326, <https://doi.org/10.1002/pip.3574>.
- [15] T.G. Allen, J. Bullock, X. Yang, A. Javey, S. De Wolf, Passivating contacts for crystalline silicon solar cells, *Nat. Energy* 4 (11) (2019) 914–928, <https://doi.org/10.1038/s41560-019-0463-6>.
- [16] A. ur Rehman, et al., Development and prospects of surface passivation schemes for high-efficiency c-Si solar cells, *Sol. Energy* 166 (2018) 90–97, <https://doi.org/10.1016/j.solener.2018.03.025>.
- [17] J. Nelson, in: *The Physics of Solar Cells*, first ed., Imperial College Press, London, UK, 2003.
- [18] F.E. Rougieroux, C. Sun, D. Macdonald, Determining the charge states and capture mechanisms of defects in silicon through accurate recombination analyses: a review, *Sol. Energy Mater. Sol. Cells* 187 (2018) 263–272, <https://doi.org/10.1016/j.solmat.2018.07.029>.
- [19] J. Junge, A. Herguth, G. Hahn, D. Kreßner-Kiel, R. Zierer, Investigation of degradation in solar cells from different mc-Si materials, *Energy Proc.* 8 (2011) 52–57, <https://doi.org/10.1016/j.egypro.2011.06.101>.
- [20] A.R. Peaker, et al., Recombination via point defects and their complexes in solar silicon, *Phys. Status Solidi* 209 (10) (2012) 1884–1893, <https://doi.org/10.1002/pssa.201200216>.
- [21] W. Shockley, W.T. Read, Statistics of the recombinations of holes and electrons, *Phys. Rev.* 87 (5) (1952) 835–842, <https://doi.org/10.1103/PhysRev.87.835>.
- [22] R.N. Hall, Electron-hole recombination in germanium, *Phys. Rev.* 87 (2) (1952), <https://doi.org/10.1103/PhysRev.87.387>, 387–387.
- [23] Y. Zhu, C. Sun, T. Nieuwelt, G. Coletti, Z. Hameiri, Investigation of two-level defects in injection dependent lifetime spectroscopy, *Sol. Energy Mater. Sol. Cells* 216 (2020) 110692, <https://doi.org/10.1016/j.solmat.2020.110692>.
- [24] C.-T. Sah, W. Shockley, Electron-hole recombination statistics in semiconductors through flaws with many charge conditions, *Phys. Rev.* 109 (4) (1958) 1103–1115, <https://doi.org/10.1103/PhysRev.109.1103>.
- [25] S. Rein, in: *Lifetime Spectroscopy: A Method of Defect Characterization in Silicon for Photovoltaic Applications*, first ed., Springer, New York, USA, 2005.
- [26] Y. Zhu, Advanced Characterization of Defects in Silicon Wafers and Solar Cells', Ph. D. Dissertation, School of Photovoltaic and Renewable Energy, UNSW, Sydney, Australia, 2019.

- [27] J.D. Murphy, K. Bothe, R. Krain, V.V. Voronkov, R.J. Falster, Parameterisation of injection-dependent lifetime measurements in semiconductors in terms of Shockley-Read-Hall statistics: an application to oxide precipitates in silicon, *J. Appl. Phys.* 111 (11) (2012) 113709, <https://doi.org/10.1063/1.4725475>.
- [28] Y. Zhu, Q.T. Le Gia, M.K. Juhl, G. Coletti, Z. Hameiri, Application of the Newton-Raphson method to lifetime spectroscopy for extraction of defect parameters, *IEEE J. Photovoltaics* 7 (4) (2017) 1092–1097, <https://doi.org/10.1109/JPHOTOV.2017.2695666>.
- [29] Y. Buratti, J. Dick, Q. Le Gia, Z. Hameiri, Deep learning extraction of the temperature-dependent parameters of bulk defects, *ACS Appl. Mater. Interfaces* 14 (41) (2022) 48647–48657, <https://doi.org/10.1021/acsami.2c12162>.
- [30] Y. Buratti, Q.T. Le Gia, J. Dick, Y. Zhu, Z. Hameiri, Extracting bulk defect parameters in silicon wafers using machine learning models, *npj Comput. Mater.* 6 (1) (2020) 142, <https://doi.org/10.1038/s41524-020-00410-7>.
- [31] Y. Buratti, J. Dick, Q.L. Gia, Z. Hameiri, A machine learning approach to defect parameters extraction: using random forests to inverse the Shockley-Read-Hall equation, in: 2019 IEEE 46th Photovoltaic Specialists Conference (PVSC), 2019, pp. 3070–3073, <https://doi.org/10.1109/PVSC40753.2019.8980717>.
- [32] I. Goodfellow, in: *Deep Learning*, first ed., The MIT Press, Cambridge, UK, 2016.
- [33] S. Raschka, V. Mirjalili, *Python machine learning: machine learning and deep learning with Python*, in: third ed. Scikit-Learn, and TensorFlow, vol. 2, Packt Publishing, Birmingham, UK, 2019. Limited.
- [34] T. Niewelt, J. Schön, J. Broisch, W. Warta, M. Schubert, Electrical characterization of the slow boron oxygen defect component in Czochralski silicon, *pss (RRL)* 9 (12) (2015) 692–696, <https://doi.org/10.1002/pssr.201510357>.
- [35] S.R. Krishnan, C.S. Seelamantula, On the selection of optimum Savitzky-Golay filters, *IEEE Trans. Signal Process.* 61 (2) (2013) 380–391, <https://doi.org/10.1109/TSP.2012.2225055>.
- [36] ASTM, ‘Standard Test Method for Interstitial Atomic Oxygen Content of Silicon by Infrared Absorption with Short baseline.’, 2003 org/10.1520/F1188-02.